AIAA 24th Fluid Dynamics Conference, July 6-9, 1993/Orlando, FL ,AIAA paper 93-2936

Reynolds Stress Transport Modelling of Shock/Boundary-Layer Interaction

Lars Davidson
Thermo and Fluid Dynamics
Chalmers University of Technology
S-412 96 Gothenburg, Sweden

Abstract

The interaction process in transonic flow between the inviscid free stream and the turbulent boundary layer is an challenging task for numerical simulation, which involves complex physical phenomena. In order to capture the physics a turbulence model capable of accounting for physical phenomena such as streamline curvature, strong nonlocal effects and history effects, and large irrotational strains should be used.

In the present work a second-moment Reynolds Stress Transport Model (RSTM) is used for computing transonic flow in a plane channel with a bump. An explicit time-marching Runge-Kutta code is used for the mean flow equations. For solving the transport equations for the Reynolds stresses $\overline{u^2}, \overline{v^2}$ and $\overline{uv}$ as well as k and ε an implicit solver is used which – unlike the Runge-Kutta solver – proved to be very stable and reliable for solving source dominated equations. Second-order discretization schemes are used for all equations. As the RSTM is valid only for fully turbulent flow, an one-equation model is used near the wall. The two models are matched along a pre-selected grid line in the fully turbulent region.

The agreement between predictions and measurements is, in general, good. The interaction between the boundary layer and the external supersonic layer is stronger than in the experiments, which may due to two factors: ahead of the shock the predicted boundary layer is thicker than the experimental one, and oscillations in the shock wave are found in the experiments.

1 Introduction

Accurate prediction of shock wave turbulent boundary-layer interactions in transonic flows is of great practical importance for many industrial applications. The computers of today are sufficiently powerful to allow us to perform Navier-Stokes calculations on fine grids and – at the same time – use second-moment closure models for the turbulence. When assessing the performance of turbulence models it is important that the configuration is as simple as possible, but that it still possesses the essential details of practical configurations. The shock/boundary-layer interaction in a two-dimensional channel with a bump – which is investigated in the present study – fulfils these requirements. This configuration was a test case in a BRITE/EURAM project on CFD-validation called EUROVAL.[1]

In the present work the transonic flow in a two-dimensional channel with a bump is calculated using a Reynolds Stress Transport Model (RSTM), which has been implemented into an existing explicit Runge-Kutta time-marching finite volume code. In order to obtain stable and convergent solutions for the equations of the turbulent quantities ($k, \varepsilon, \overline{u^2}, \overline{v^2}$ and $\overline{uv}$), they are solved with an implicit solver. In the viscosity dominated flow near the wall ($y^+ \leq 50$), the RSTM is matched with a one-equation model.

Second-moment closures such as RSTM are superior to simpler turbulence models such as the $k - \varepsilon$ or the Baldwin-Lomax models. The main reasons for their superiority are their ability to account for *i)* streamline curvature, *ii)* strong nonlocal effects and history effects for the individual stresses, and *iii)* irrotational strains, phenomena which all are present in shock/boundary-layer interaction.

i) When the streamlines of the mean flow have a convex (concave) curvature the turbulence is stabilised (destabilised), which dampens (augments) the turbulence,[2,3] especially the shear stress and the Reynolds stress normal to the wall. Bradshaw[2] demonstrates that even small amounts of convex curvature can have significant effect on the turbulence. In the present configuration both wall curvature and streamline curvature are present.

ii) The shock produces strong anisotropy in the Reynolds stresses which is transported downstream.

---

iii) In boundary layer flow the only term which contributes to the production term in the k-equation is $-\rho\overline{uv}\partial U/\partial y$ (x denotes streamwise direction). Thompson and Whitelaw[4] found that near the separation point, as well as in the separation zone, the production term $-\rho(\overline{u^2} - \overline{v^2})\partial U/\partial x$ is of equal importance. This is also the case for transonic flow where large irrotational strains $(\partial U/\partial x, \partial V/\partial y)$ prevail in, for example, the shock region.

The interaction process between the inviscid free stream and the turbulent boundary layer involves complex physical phenomena. When a shock penetrates into a boundary layer, the Mach number of the upstream flow it encounters gets lower as the shock approaches the wall. The shock must adapt itself to this situation so that it vanishes when it reaches sonic conditions. The pressure signal carried by the shock is transmitted in the upstream direction when the Mach number in the inner part of the boundary layer gets below one. Thus, in the inner part of the boundary layer the information of a sharp pressure increase caused by the shock is transmitted upstream. This causes a thickening of the boundary layer, which generates compression waves in the adjacent supersonic layer. These waves will in turn weaken the shock. If the shock is strong enough an oblique shock is produced by the coalescence of the compression waves, giving a so-called λ-shock.

Several novel features are presented in the present paper:

- a RSTM implemented in a time-marching, compressible code;
- Reynolds transport stress modelling in transonic flow;
- the RSTM is coupled with a one-equation model in the viscosity dominated region near the wall;
- an implicit ADI-solver is employed for the turbulent quantities, which removes the convergence problems experienced with the Runge-Kutta solver.

The first part of the paper outlines the numerical method for solving the mean-flow equations, the second part presents the RSTM. After that follows a section where it is shown how second-moment closures *do* respond to streamline curvature effects as well as irrotational strains. The final part presents an extensive comparison of computations and experiments including mean velocities, wall Mach number, turbulent shear- and normal stresses.

2 Mean Flow Equations

The numerical scheme applied to solve the mean-flow equations belongs to the class of explicit Runge-Kutta schemes with central finite-volume differencing and adaptive artificial viscosity, and this particular one has been reported before.[5–7] The mean flow equations in Cartesian coordinates over a control volume V with boundary ∂V read

$$\frac{\partial}{\partial t}\iiint_V \mathbf{U}\,dV + \iint_{\partial V} \mathcal{H}(\mathbf{U})\cdot\mathbf{n}dS = 0 \qquad (1)$$

where the vector of state variables $\mathbf{U} = (\rho \;\; \rho U \;\; \rho V \;\; \rho E)^T$ contains density ρ, x, and y components of mean-flow velocity U, V, and energy per unit mass E. The flux tensor $\mathcal{H}$ is composed of inviscid, viscous and turbulent parts

$$\mathcal{H} = (F_I - F_V - F_T)\mathbf{e}_x + (G_I - G_V - G_T)\mathbf{e}_y \qquad (2)$$

in the x, and y coordinate directions, respectively.

The inviscid fluxes are given by

$$F_I = \begin{pmatrix} \rho U \\ \rho U^2 + p \\ \rho UV \\ \rho UH \end{pmatrix}, \quad G_I = \begin{pmatrix} \rho V \\ \rho UV \\ \rho V^2 + p \\ \rho VH \end{pmatrix} \qquad (3)$$

and the viscous and turbulent fluxes are given by

$$F_V + F_T = \begin{pmatrix} 0 \\ \tau_{xx} - \rho\overline{u^2} \\ \tau_{xy} - \rho\overline{uv} \\ U\left(\tau_{xx} - \rho\overline{u^2}\right) + V\left(\tau_{yx} - \rho\overline{uv}\right) - q_x \end{pmatrix},$$

$$G_V + G_T = \begin{pmatrix} 0 \\ \tau_{yx} - \rho\overline{uv} \\ \tau_{yy} - \rho\overline{v^2} \\ U\left(\tau_{xy} - \rho\overline{uv}\right) + V\left(\tau_{yy} - \rho\overline{v^2}\right) - q_y \end{pmatrix},$$

H is the stagnation enthalpy, $H = E + p/\rho$, and p is the static pressure.

Components of the viscous stress tensor are,

$$\tau_{xx} = \tfrac{2}{3}\mu\left(2\tfrac{\partial U}{\partial x} - \tfrac{\partial V}{\partial y}\right) \qquad \tau_{xy} = \tau_{yx} = \mu\left(\tfrac{\partial U}{\partial y} + \tfrac{\partial V}{\partial x}\right)$$
$$\tau_{yy} = \tfrac{2}{3}\mu\left(2\tfrac{\partial V}{\partial y} - \tfrac{\partial U}{\partial x}\right)\;. \qquad (4)$$

The heat flux terms in the energy equation are not calculated with RSTM, but the eddy viscosity assumption is used, i.e.

$$q_x = -\left(\frac{\mu}{Pr} + \frac{\mu_t}{Pr_t}\right)\frac{\partial T}{\partial x} \qquad q_y = -\left(\frac{\mu}{Pr} + \frac{\mu_t}{Pr_t}\right)\frac{\partial T}{\partial y}$$

where the turbulent viscosity is obtained from k and ε as

$$\mu_t = c_\mu \rho \frac{k^2}{\varepsilon}$$

The value of the Prandtl number $Pr = \mu C_p/k$ was taken as a constant 0.72, and Pr_t was set to 0.9 (constant) for the turbulent flow solutions presented in this paper. The laminar viscosity μ is calculated using the Sutherland formula.

The main features of the finite volume code can be summarised as:

- explicit, compressible time-marching, cell-centered, central differencing, local time stepping;
- four stage Runge-Kutta scheme for the mean flow equations;
- the $\overline{u^2}, \overline{v^2}, \overline{uv}, k$ and ε equations are solved using a semi-implicit solver (ADI);[8] the convective terms are discretized using a second-order scheme of van Leer;[9]
- fourth-order numerical non-homogeneous dissipation term in all mean flow equations scaled with the local Mach-number in order to reduce the numerical dissipation in boundary layers; note that no second-order shock-capturing dissipation term is used.

2.1 Boundary Conditions

2.1.1 Inlet

Total temperature and total pressure are prescribed. V is set to zero and the density is extrapolated from inside. The U-velocity and the total energy are set as:

$$\begin{aligned} U &= \sqrt{2RT_o \left[1 - \left(\frac{p}{p_o}\right)^{\gamma-1}\right] \frac{\gamma}{\gamma-1}} \\ E_o &= \frac{p}{\rho(\gamma-1)} + \frac{1}{2}(U^2+V^2) \end{aligned}$$

All turbulent quantities are set to small values.

2.1.2 Outlet

The pressure is fixed at the outlet. For the remaining variables the Riemann invariants are used, which are based on the theory of characteristics for the locally one-dimensional problem. The four Riemann invariants are:

$$\begin{aligned} R_1 &= \mathbf{U}\cdot\mathbf{n} - \frac{2}{\gamma-1}c \\ R_2 &= \mathbf{U}\cdot\mathbf{n} + \frac{2}{\gamma-1}c \\ R_3 &= \ln(\frac{p}{\rho^\gamma}) \\ R_4 &= n_y U - n_x V \end{aligned}$$

where $\mathbf{n}$ and c denote normal vector and speed of sound, respectively. The normal gradients of the Riemann invariants are set to zero, i.e.

$$\frac{\partial R_m}{\partial n} = 0$$

R_1 is taken from outside and R_2, R_3 and R_4 from inside (outside and inside refer to the calculation domain). R_3 gives the density since the pressure p/p_o is given at the outside. R_4 gives the tangential velocity V. Finally, knowing the speed of sound both inside and outside, R_2 gives the U-velocity.

Due to three-dimensional effects in the experimental setup (see Section 5), the outlet pressure has to be modified so that the predicted shock position agrees with the experimental one. The outlet pressure $p/p_0 = 0.652$ was used.

2.1.3 Wall

The normal gradients for temperature and pressure are set to zero, and the remaining variables are set to zero.

2.1.4 Symmetry Line

V is set to zero, and the normal gradient is set to zero for the remaining variables.

3 The Reynolds Stress Transport Model

When computing compressible flow either mass-averaging (compressible) or time-averaging (incompressible) variables can be used. In weakly compressible flow (Mach-number below 2), as in the present study, the incompressible time-averaging concept can be used.

The Reynolds Stress Transport Model neglecting compressibility has the form:[10]

$$\underbrace{\frac{\partial}{\partial x_k}\left(\rho U_k \overline{u_i u_j}\right)}_{\text{convection}} = \underbrace{-\rho\overline{u_i u_k}\frac{\partial U_j}{\partial x_k} - \rho\overline{u_j u_k}\frac{\partial U_i}{\partial x_k}}_{\text{production } P_{ij}} \tag{5}$$
$$+ \quad \Phi_{ij} + D_{ij} - \rho\varepsilon_{ij}$$

The convection and production terms are exact and do not need any modelling assumptions. The pressure strain Φ_{ij} and the dissipation ε_{ij} are modelled as:

$$\begin{aligned}
\Phi_{ij} &= \Phi_{ij,1} + \Phi_{ij,2} + \Phi_{ij,w1} + \Phi_{ij,w2} \\
\Phi_{ij,1} &= -c_1\rho\frac{\varepsilon}{k}\left(\overline{u_i u_j} - \frac{2}{3}\delta_{ij}k\right) \\
\Phi_{ij,2} &= -c_2\left(P_{ij} - \frac{2}{3}\delta_{ij}P_k\right) \\
P_k &= \frac{1}{2}P_{jj} \\
\Phi_{ij,w1} &= c_1'\frac{\varepsilon}{k}(\overline{u_k u_m}n_k n_m\delta_{ij} \\
&- \frac{3}{2}\overline{u_k u_i}n_k n_j - \frac{3}{2}\overline{u_k u_j}n_i n_k)\left(\frac{\ell_t}{x_n}\right) \\
\Phi_{ij,w2} &= c_2'\frac{\varepsilon}{k}(\Phi_{km,2}n_k n_m\delta_{ij} \\
&- \frac{3}{2}\Phi_{ik,2}n_k n_j - \frac{3}{2}\Phi_{kj,2}n_i n_k)\left(\frac{\ell_t}{x_n}\right) \\
\varepsilon_{ij} &= \frac{2}{3}\delta_{ij}\varepsilon
\end{aligned}$$

The f-function is a damping function which reduces the effect of the wall correction with increasing distance x_n (n denotes normal direction), and which has the form $f = k^{3/2}/(2.55x_n\varepsilon)$.

The diffusion term D_{ij} is modelled using the Generalized Gradient Diffusion Hypothesis GGDH[11]

$$D_{ij} = \frac{\partial}{\partial x_m}\left(c_s\rho\overline{u_k u_m}\frac{k}{\varepsilon}\frac{\partial\Phi}{\partial x_k}\right) \tag{6}$$

with $\Phi = \overline{u_i u_j}$. A simpler eddy viscosity assumption

$$D_{ij} = \frac{\partial}{\partial x_m}\left(\frac{\mu_t}{\sigma_t}\frac{\partial\Phi}{\partial x_m}\right)$$

where the turbulent Prandtl number σ_t is equal to one, was also tested. The difference in the obtained results using the two diffusion model was found to be negligible.

The Reynolds stresses are stored at the cell centres. In implicit SIMPLE codes apparent viscosity are used in the momentum equations to enhance stability via stability-promoting second derivatives.[12] When using Runge-Kutta solvers for the momentum equations, no such stability promoting remedies are needed, because the mean flow variables are solved *explicitly*, which means that all terms are at the right-hand-side of the discretized equations, and thus the solution procedure is not sensitive to the explicit adding of the Reynolds stresses.

3.1 Near Wall Modelling

Near the walls the one-equation model by Wolfshtein,[13] modified by Chen and Patel,[14] is used. In this model the standard k equation is solved; the diffusion term in the k-equation is modelled using the eddy viscosity assumption. The turbulent length scales are prescribed as:

$$\ell_\mu = c_\ell n\left[1 - exp\left(-R_n/A_\mu\right)\right],\ \ \ell_\varepsilon = c_\ell n\left[1 - exp\left(-R_n/A_\varepsilon\right)\right]$$

(n is the normal distance from the wall) so that the dissipation term in the k-equation and the turbulent viscosity are obtained as:

$$\varepsilon = \frac{k^{3/2}}{\ell_\varepsilon},\ \ \mu_t = c_\mu\rho\sqrt{k}\ell_\mu \tag{7}$$

The Reynolds number R_n and the constants are defined as

$$R_n = \frac{\sqrt{k}n}{\nu},\ c_\mu = 0.09,\ \ c_\ell = \kappa c_\mu^{-3/4},\ \ A_\mu = 70,\ \ A_\varepsilon = 2c_\ell$$

The one-equation model is used near the walls (for $R_n \leq 250$; the matching line is chosen along a preselected grid line), and the standard high-Re RSTM in the remaining part of the flow. No special boundary condition is needed at the interface. The stresses computed near the matching line in the one-equation region are used as boundary conditions for the stress equations, and turbulent stresses are naturally transported (by convection and diffusion) across the matching line.

The matching of the one-equation model and the k and ε-equations does not pose any problems but gives a smooth distribution of μ_t and ε across the matching line. If the Reynolds stresses in the one-equation region are computed from Boussinesq approximation it gives rise to non-continuity in the Reynolds stresses across the matching line,[7] since the one-equation model gives more or less isotropic normal Reynolds stresses, whereas RSTM gives highly non-isotropic Reynolds stresses, which results in a jump in the profiles of $\overline{u^2}$ and $\overline{v^2}$ across the matching line. This problem is less serious for the shear stress. In the present study the stresses in the one-equation region are computed as:

$$\rho\overline{uv} = -\mu_t \left(\frac{\partial U}{\partial y} + \frac{\partial V}{\partial x} \right)$$

$$\rho\overline{u^2} = \rho k \left(\frac{\overline{u^2}}{k} \right)_{\text{outer}}$$

$$\rho\overline{v^2} = \rho k \left(\frac{\overline{v^2}}{k} \right)_{\text{outer}}$$

where μ_t is calculated using Eq. 7, and $(\overline{u^2}/k)_{\text{outer}}$ and $(\overline{v^2}/k)_{\text{outer}}$ are the ratios of $\overline{u^2}$, $\overline{v^2}$ and k just outside the matching line, and these ratios are supposed to remain constant all the way to the wall. In this way the distribution of the stresses is smooth across the matching line. It seems, however, that the velocity field is fairly insensitive to the treatment of the normal stresses in the one-equation region.

3.2 The k and ε-equations

In a RSTM there are two equivalent sets of equations which can be solved. Either $\overline{u^2}, \overline{v^2}, \overline{w^2}, \overline{uv}$ and ε or $\overline{u^2}, \overline{v^2}, k, \overline{uv}$ and ε. The latter set has been chosen in the present study. The main reason for this choice is that the k-equation has to be solved anyway in the one-equation region.

The standard k and ε-equations in the RSTM have the form:

$$\begin{aligned} \frac{\partial}{\partial x_j}\left(\rho U_j k\right) &= D_k + P_k - \rho\varepsilon \\ \frac{\partial}{\partial x_j}\left(\rho U_j \varepsilon\right) &= D_\varepsilon + \frac{\varepsilon}{k}\left(c_{1\varepsilon} P_k - c_{2\varepsilon}\rho\varepsilon\right) \end{aligned}$$

The diffusion term D_k, D_ε are, as for the Reynolds stresses, calculated using GGDH, see Eq. (6).

The constants have been assigned values according to Gibson and Younis:[15]

$(c_1, c_2, c_1', c_2', c_s, c_\varepsilon, c_{1\varepsilon}, c_{2\varepsilon})$=(3, 0.3, 0.75, 0.15, 0.22, 0.18, 1.4, 1.8)

3.3 Solver

In Ref. 7, attempts were carried out to solve the k and ε equations explicitly using the existing Runge-Kutta solver. However, no stable, convergent solution was obtained. Instead an implicit discretization method using an ADI-solver has been employed, which has been used for the last 30 years in incompressible codes based on pressure-correction procedures such as SIMPLE.[16,17] For more details, see Refs. 7,8.

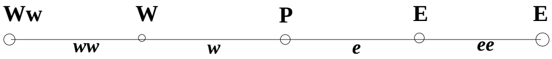

Figure 1: *A simplified one-dimensional grid.*

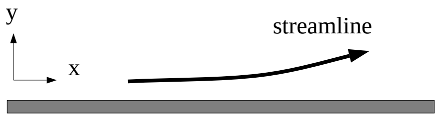

Figure 2: *The streamlines, which in flat-plate boundary layers are along the x-axis, are suddenly deflected upwards (concave curvature) due to, e.g., an approaching shock.*

Central differencing is employed for the diffusive terms, and for the convective terms a scheme of Van Leer[9] is used. The van Leer scheme is bounded and of second-order accuracy, except at local minima or maxima where its accuracy is of the first order. The scheme can be considered as a first-order upwind scheme with a correction term which gives it second-order accuracy. For the west face it can be written as (see Fig. 1)

when $U_w > 0$:

$$\begin{array}{ll} \text{if} & |\Phi_P - 2\Phi_W + \Phi_{Ww}| \ \geq \ |\Phi_P - \Phi_{Ww}| \\ \text{then} & \Phi_w = \Phi_W \\ \text{else} & \Phi_w = \Phi_W + (\Phi_P - \Phi_W)\,\dfrac{(\Phi_W - \Phi_{Ww})}{(\Phi_P - \Phi_{Ww})}; \end{array}$$

when $U_w < 0$:

$$\begin{array}{ll} \text{if} & |\Phi_W - 2\Phi_P + \Phi_E| \ < \ |\Phi_W - \Phi_E| \\ \text{then} & \Phi_w = \Phi_P \\ \text{else} & \Phi_w = \Phi_P + (\Phi_W - \Phi_P)\,\dfrac{(\Phi_P - \Phi_E)}{(\Phi_W - \Phi_E)}. \end{array}$$

4 The Effects of Streamline Curvature and Irrotational Strains

Second-moment closures such as RSTM are superior to simpler turbulence models such the $k - \varepsilon$ and the Baldwin-Lomax models. Two of the reasons (see Introduction) for the superiority of the RSTM are its ability of taking into account the influence of 1) streamline curvature and 2) normal stresses and irrotational strains. The physics of both these phenomena are faithfully reproduced by second-moment closures because the production terms need not to be modelled.

	$\partial \mathbf{U}_\theta/\partial \mathbf{r} > 0$	$\partial \mathbf{U}_\theta/\partial \mathbf{r} < 0$
convex curvature	stabilising	destabilising
concave curvature	destabilising	stabilising

Table 1: *Effect of streamline curvature on turbulence.*

4.1 Streamline Curvature

When the streamlines of the mean flow have a convex curvature the turbulence is stabilised, which dampens the turbulence,[2,3] especially the shear stress and the Reynolds stress normal to the wall. Concave curvature destabilises the turbulence. The ratio of boundary layer thickness δ to curvature radius R, δ/R, is a common parameter for quantifying the curvature effects on the turbulence. The work reviewed by Bradshaw[2] demonstrates that even such small amounts of convex curvature as $\delta/R = 0.01$ can have significant effect on the turbulence. Thompson and Whitelaw[4] carried out an experimental investigation on a configuration simulating the flow near a trailing edge of an airfoil, where they measured $\delta/R \simeq 0.03$. They report a 50 percent decrease of $\rho\overline{v^2}$ (Reynolds stress in the normal direction to the wall) due to curvature. The reduction of $\rho\overline{u^2}$ and $-\rho\overline{uv}$ were substantial as well. They also report significant damping of the turbulence in the shear layer in the outer part of the separation region.

Assume we have a flat-plate boundary layer flow. The ratio of the normal stresses $\rho\overline{u^2}$ and $\rho\overline{v^2}$ is typically 5. At one x-station the flow is deflected upwards, see Fig. 2. How will this affect the turbulence? Let us study the effect of concave streamline curvature. The production terms P_{ij} in Eq. 5 due to rotational strains can be written

$$\text{RSTM}, \overline{u^2}-\text{eq.} \quad : \quad P_{11} = -2\rho\overline{uv}\frac{\partial U}{\partial y}$$

$$\text{RSTM}, \overline{uv}-\text{eq.} \quad : \quad P_{12} = -\rho\overline{u^2}\frac{\partial V}{\partial x} - \rho\overline{v^2}\frac{\partial U}{\partial y}$$

$$\text{RSTM}, \overline{v^2}-\text{eq.} \quad : \quad P_{22} = -2\rho\overline{uv}\frac{\partial V}{\partial x}$$

$$k-\varepsilon \quad : \quad P_k = \mu_t\left(\frac{\partial U}{\partial y} + \frac{\partial V}{\partial x}\right)^2$$

As long as the streamlines in Fig. 2 are parallel to the wall, all production is due to $\partial U/\partial y$, but as soon as the streamlines are deflected we get more terms due to $\partial V/\partial x$. Even if $\partial V/\partial x$ is much smaller than $\partial U/\partial y$ it will still give a non-negligible contribution to P_{12} since $\rho\overline{u^2}$ is much larger than $\rho\overline{v^2}$. Thus the magnitude of P_{12} will increase (P_{12} is negative) since $\partial V/\partial x > 0$. An increase of the magnitude of P_{12} will increase $-\overline{uv}$, which, in turn, will increase P_{11} and P_{22}. This means that $\rho\overline{u^2}$ and $\rho\overline{v^2}$ will be larger and the magnitude of P_{12} will be further increased, and so on. It is seen that we have a positive feedback, which continuously increases the Reynolds stresses. We say that the turbulence is *destabilised* due to concave curvature of the streamlines.

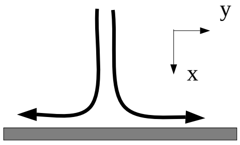

Figure 3: *Stagnation flow.*

However, the $k-\varepsilon$ model is not very sensitive to streamline curvature, since the two rotational strains are multiplied with the same coefficient (the turbulent viscosity).

If the flow in Fig. 2 is a wall-jet flow where $\partial U/\partial y < 0$ the situation will be reversed: the turbulence will be *stabilised*. If the streamline (and the wall) in Fig. 2 is deflected downwards the situation will be as follows: the turbulence is stabilising when $\partial U/\partial y > 0$, and destabilising for $\partial U/\partial y < 0$.

If streamline curvature has a stabilising or destabilising effect is thus dependent on type of curvature (convex or concave), and if momentum in the tangential direction increases or decreases with radial distance from its origo (i.e. the sign of $\partial U_\theta/\partial r$). For convenience these cases are summarised in Table 1.

4.2 Irrotational Strains

In pure boundary layer flow the only term which contributes to the production term in the k and ε-equations is $-\rho\overline{uv}\partial U/\partial y$. Thompson and Whitelaw[4] found that near the separation point, as well as in the separation zone, the production term $-\rho(\overline{u^2}-\overline{v^2})\partial U/\partial x$ is of equal importance. This is also the case for transonic flow where large irrotational strains ($\partial U/\partial x, \partial V/\partial y$) prevail in the shock region as well as in separated flow regions. As the exact form of the production terms are used in second-moment closures, the production due to irrotational strains is correctly accounted for.

In the case of stagnation-like flow (see Fig. 3), where $\overline{u^2} \simeq \overline{v^2}$ the production due to normal stresses is zero,

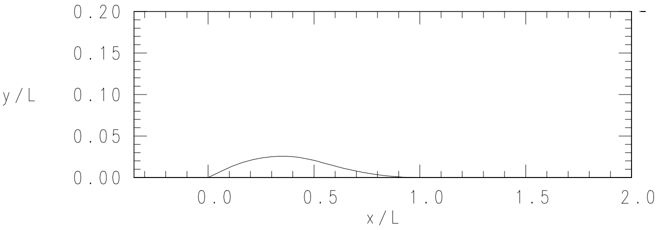

Figure 4: *Configuration of the channel with a bump. Left boundary: inlet; right boundary: outlet; upper boundary: symmetry line; lower boundary: wall.*

which is also the results given by second-moment closure, whereas $k-\varepsilon$ models give a large production. In order to illustrate this, let us write the production due to the irrotational strains $\partial U/\partial x$ and $\partial V/\partial y$ for RSTM and $k-\varepsilon$:

$$\begin{aligned} RSTM &: \quad 0.5\,(P_{11}+P_{22}) = -\rho\overline{u^2}\frac{\partial U}{\partial x} - \rho\overline{v^2}\frac{\partial V}{\partial y} \\ k-\varepsilon &: \quad P_k = 2\mu_t\left\{\left(\frac{\partial U}{\partial x}\right)^2 + \left(\frac{\partial V}{\partial y}\right)^2\right\} \end{aligned}$$

If $\overline{u^2} \simeq \overline{v^2}$ we get $P_{11}+P_{22} \simeq 0$ since $\partial U/\partial x = -\partial V/\partial y$ due to continuity (nearly incompressibe). The production term P_k in $k-\varepsilon$ model, however, will be large, since it will be *sum* of the two strains.

5 Results

The configuration is shown in Fig. 4. A number of different meshes have been tested including meshes with 202 × 64 nodes, 101 × 101 nodes, and two meshes with 101 × 64 nodes with different spacing in the y-direction. It was found that all meshes gave virtually identical results leading to the conclusion that the calculated fields are grid independent. The coefficient in front of the fourth-order numerical dissipation was also varied in order to verify that the numerical diffusion had no adverse effects on the predictions. All results presented below has been carried out with a 101 × 64-node mesh. Grid lines are concentrated in the shock region and near the wall (the first grid line near the wall is located at $y^+ \simeq 2$). One advantage of using a one-equation model compared to using a standard low-Re model where ε is solved all the way to the wall, is that the former model does need as fine grid near walls. When solving for ε a very fine grid is needed near the walls in order to resolve the steep gradients of ε.

The predicted results are compared with detailed laser velocimetri data of Délery and his group.[19,18] The Mach number at the inlet is approximately 0.6, the flow is accelerated over the bump and reaches supersonic conditions with $Ma \simeq 1.3$ just in front of the shock at $x/L \simeq 0.8$. After the shock the experimental flow exhibits incipient separation.

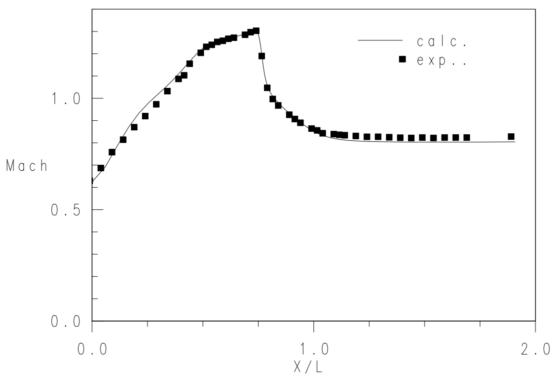

Figure 6: *Isentropic Mach number at the lower wall.*

The exit pressure in the experiments was $p_{exit}/p_0 = 0.64$. If this value is used, the shock is predicted too late. The same conclusions was drawn in EUROVAL[1] and by Dimitriades & Leschziner[20] and Lien.[21] It should be noted that the post-shock pressure is below that given by inviscid theory for a normal shock, which indicates that the cross-section area is reduced in some way, e.g. by growing boundary layers on the lateral walls causing three-dimensional effects as suggested in Refs. 1, 20, 21, or, as proposed by Délery and Marwin,[23] through the rapid increase of the thickness of the boundary layers at the upper and lower walls. The reason for the low pressure after the shock is probably a combination of the two effects. In the calculations the exit pressure has been set to $p_{exit}/p_0 = 0.652$ so as to give the shock at the experimental position.

Contours of constant Mach numbers are shown in Fig. 5. It can be seen that shock occurs at $x/L \simeq 0.8$ and there is no clear λ-structure, indicating a relatively weak interaction between the shock and the turbulent boundary layer.

In Fig. 6 the calculated isentropic Mach number at the wall is compared with experiments. It can be seen that after the shock the predicted Mach number is smaller (the pressure is larger) than the experimental one. This is because the exit pressure has been increased in the calculations in order to obtain the shock position according to experiments.

The predicted U-velocities and the Reynolds stresses (divided by density) are compared with experiments in Figs. 7-10 (all velocities have been made non-dimensional with the stagnation speed of sound a_0, and x, y have been made non-dimensional with the length of the bump L). From the U-profiles it is seen that well ahead of the shock ($x/L = 0.65$) the predicted boundary layer is thicker than the experimental one.

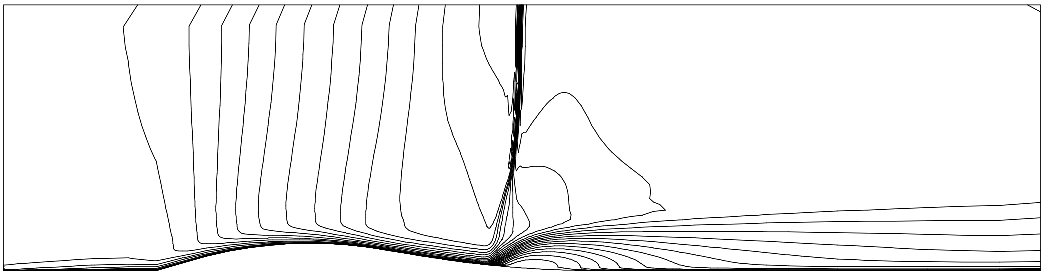

Figure 5: Contours of constant Mach numbers.

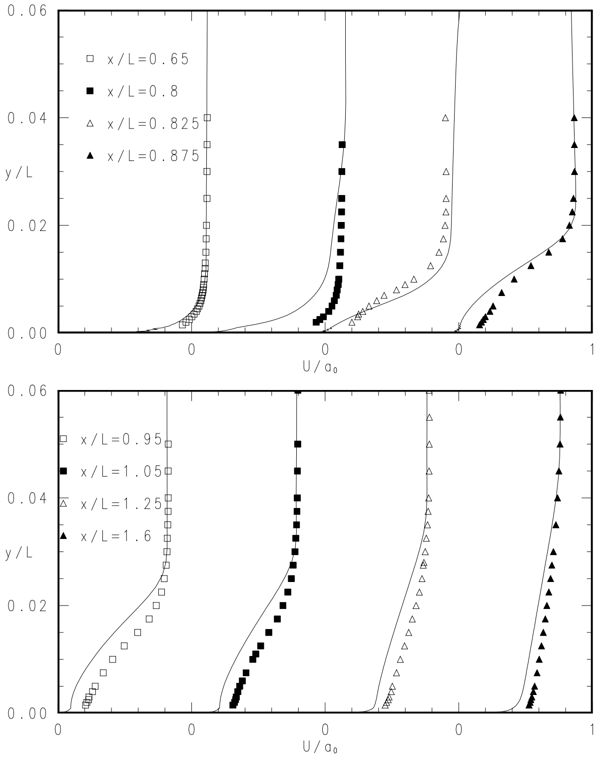

Figure 7: *U-velocities. Solid lines: predictions; markers: experiments.*

The predicted Reynolds stresses, however, are in good agreement with the experimental ones. The velocity profile at $x/L = 0.8$ shows that the flow in the lower part of the channel ($y/L < 0.055$) has not yet entered the shock region, whereas further away from the wall the flow has reached the shock. In the shock region on an airfoil, Alber *et al.*[27] found similar velocity profiles. This is due to the interaction process between the boundary layer and the external flow. The information of an approaching shock is transmitted upstream in the subsonic part of the boundary layer, which causes a thickening of the boundary layer. This thickening generates, in turn, compression waves in the outer supersonic region. As a result the shock-wave becomes inclined and the width of the shock region is increased, see Fig. 5.

After the shock the predicted velocity profiles show more tendency to separate than the experimental ones illustrating a stronger interaction between the shock and the turbulent boundary layer in the predictions than in the experiments. This is probably due to three-dimensional effects in the experiments and due to the thicker predicted boundary layer ("emptier" velocity profile) ahead of the shock. Generally, velocity profiles with low value of the form factor H_{12} ("full" boundary layer velocity profiles) has greater resistance against separation compared to profiles with high H_{12}. However, this resistance is somewhat reduced because the interaction length L^* (the distance between the point where the wall pressure starts to rise and the point where the wall Mach number falls to one) increases for increasing H_{12}.[23] Such an increase in L^* leads to a decrease of the adverse pressure gradient, since the supersonic compression takes place over a longer distance, which limits the tendency of separation. The velocity profiles in Fig. 6 seem to confirm that the interaction length is longer in the calculations than in the experiments.

In Fig. 11 the predicted displacement thickness is compared with experiments, and it is seen that the predicted interaction is much stronger than the experimental one. The predicted results shown in Figs. 6-11 are essentially the same as those presented in Refs. 24, 25,

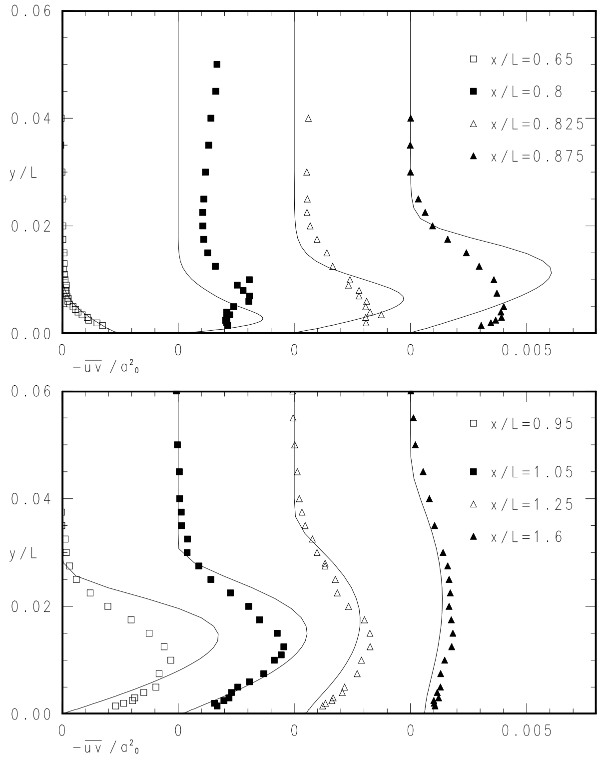

Figure 8: *$\overline{uv}$-correlations. Solid lines: predictions; markers: experiments.*

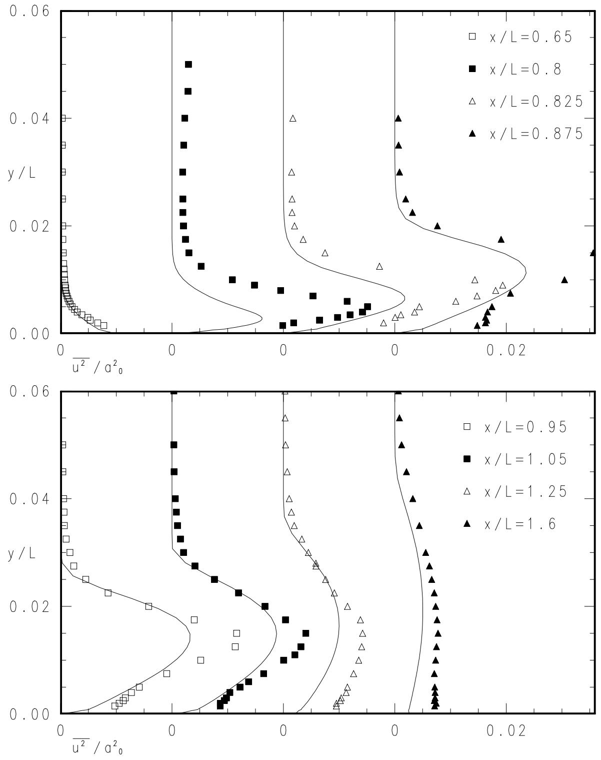

Figure 9: *$\overline{u^2}$-fluctuations. Solid lines: predictions; markers: experiments.*

where algebraic stress models (ASM) were used.

The velocity profiles in the recovery region suggest that the predicted recovery rate is too slow compared with experiments (Fig. 6 at $x/L = 1.6$), and the predicted shear stresses are too small. This is not the case as seen in Fig. 8. The predicted recovery is not too *slow*, but merely *delayed*, because of history effects from the shock region, where the predicted flow shows much stronger tendencies to separation than the experimental flow.

Oscillations in the experimental shock-wave are reported[26] (see below), which may be another reason to why the predicted interaction is stronger than the experimental one. These oscillations increase the exchange of momentum and stabilise the boundary layer, reducing tendencies to separation.

From the predicted skin friction in Fig. 12 (unfortunately no experimental data on C_F exist) it is seen that a small separation region is formed after the shock. The predicted separation region is, however, extremely thin and its vertical extension is limited to the viscous sublayer.

The predicted shear stresses in the shock region are larger than in the experiments which seems logical as the predicted velocity gradients are larger, thus generating higher $-\rho\overline{uv}$-stresses. Turning to the normal Reynolds stresses it is striking how large is the experimental level of anisotropy in the shock region. It is increasing from $\overline{u^2}/\overline{v^2} \simeq 5$ at $x/L = 0.65$ to its maximum of 12 at $x/L = 0.875$. The corresponding level of predicted anisotropy increases from 3 to maximum of 3.5 at $x/L = 0.875$. The experimental value of 12 is surprisingly high. Délery[19] argues that the cause for the large values of anisotropy can be found by studying the production terms in the $\overline{u^2}$ and $\overline{v^2}$-equations, which read:

$$\overline{u^2} - \text{eq.} \quad : \quad P_{11} = -2\rho\overline{uv}\frac{\partial U}{\partial y} - 2\rho\overline{u^2}\frac{\partial U}{\partial x} \qquad (8)$$

$$\overline{v^2} - \text{eq.} \quad : \quad P_{22} = -2\rho\overline{uv}\frac{\partial V}{\partial x} - 2\rho\overline{v^2}\frac{\partial V}{\partial y} \qquad (9)$$

In the shock region $\partial U/\partial x$ is large and negative, which means that the second term in Eq. 8 increases the production P_{11}, and the second term in Eq. 9 gives a negative contribution to P_{22}, since $\partial V/\partial y = -\partial U/\partial x$ (nearly incompressible) which reduces $\overline{v^2}$. Hence, the anisotropy *should* increase at the shock, but the question is should the increase be as strong as indicated in the experiments. In Fig. 13 the peak values of $u' \equiv \sqrt{\overline{u^2}}/a_0$ and v' are compared with experiments. The predicted $(u')_{peak}$ and $(v')_{peak}$ reach their maximum at almost the same x-station ($x/L \simeq 0.94$), but it

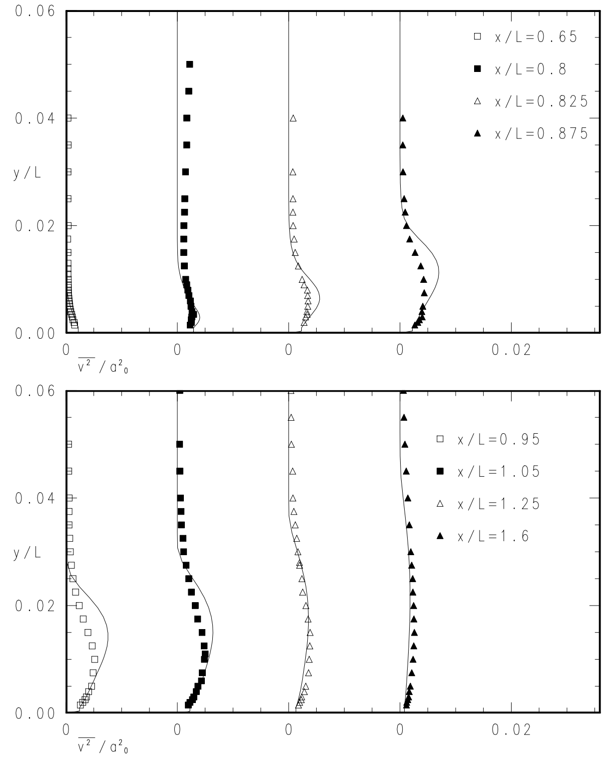

Figure 10: $\overline{v^2}$*-fluctuations. Solid lines: predictions; markers: experiments.*

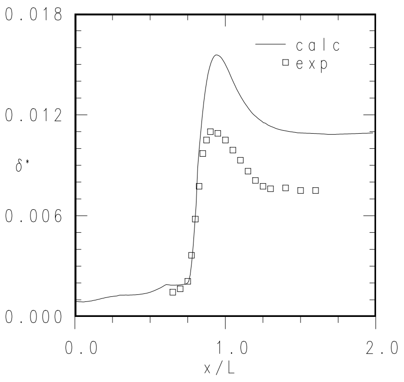

Figure 11: *Displacement thickness. Solid lines: predictions; markers: experiments.*

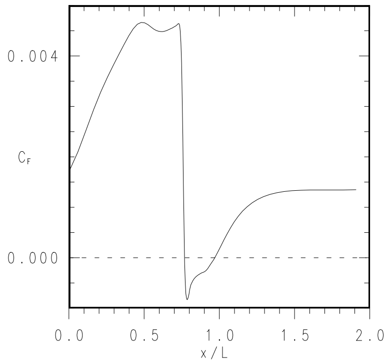

Figure 12: *Predicted skin friction along the lower wall.*

is seen that the increase towards the maximum is much more rapid for u'_{peak} than for v'_{peak}, as dictated by Eqs. 8,9. In the experiments the maximum of u'_{peak} occurs approximately $x/L = 0.05$ ahead of that of v'_{peak}.

In a later paper by Délery and his group[26] they indicate the existence of oscillations of the shock-wave, which acts as a turbulence amplifier. These oscillations appear as fluctuations in the x-direction which amplify $\overline{u^2}$ more than $\overline{v^2}$. Note that the peak values of u' in Fig. 13 are very irregular in the shock region, which enforces the conclusion reached in Ref. 26 that shock-oscillations are included in the measured $\overline{u^2}$. However, it should be mentioned that other experimental investigations also report very high turbulent fluctuations and large anisotropies in the normal stresses. Seegmiller *et al.*[28] report turbulent kinetic energies of $k/a_0^2 \simeq 0.12$ on an airfoil in the immediate post-shock region. Johnson and Bachalo,[29] who studied transonic flow on a symmetrical airfoil, present anisotropies of $\overline{u^2}/\overline{v^2} \simeq 5.8$ at 67 percent of the chord (the shock is located at x/c=0.37). If this means that shock-oscillations also exist in the experiments presented in Refs. 28, 29 is an open question.

In Fig. 14 the predicted production of turbulence in the shock region due to shear stresses are compared with experiments. It is seen that the predicted production – except at $x/L = 0.825$ – is approximately twice as large as the experimental production, which was to be expected since both the predicted $\partial U/\partial y$ as well as $-\overline{uv}$ are larger than the experimental values. This reflects, again, that the interaction in the shock region is stronger in the predictions.

The predicted production stemming from normal Reynolds stresses is also included in Fig. 15 (unfortunately the experimental counterpart could not be included becauses neither $\partial U/\partial x$ nor $\partial V/\partial y$ could be extracted from the experimental data with sufficiently high accuracy). It can be seen that near the shock ($x/L = 0.825$ and $x/L = 0.85$) the normal stresses are indeed important for the production of turbulence and that their contribution is approximately 40 % of that of the shear stresses. In Délery's paper[19] – where they apparently managed to compute $\partial U/\partial x$ – it is shown that the experimental contribution due to normal stresses is as large as the contribution due to $-\overline{uv}$.

6 Conclusions

In the present paper transonic computations of the flow in a plane channel with a bump are performed. The flow at the inlet is subsonic ($Ma \simeq 0.6$), accelerates

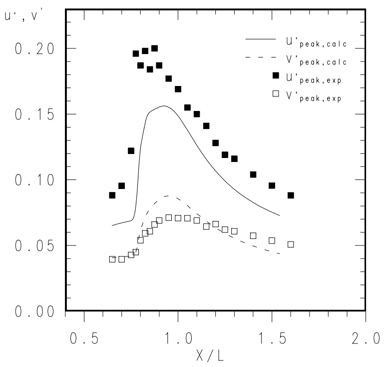

Figure 13: *Comparison of predicted and measured peak values of turbulent intensities* $u' \equiv \left(\overline{u}^2\right)^{\frac{1}{2}}/a_0$ *and* v'. *Solid line,* u'*; dashed line,* v'*;* $\square, u'_{exp}$*;* $\blacksquare$, v'_{exp}

over the bump and reaches a maximum Mach number of $Ma \simeq 1.3$ where a shock occurs. In the interaction region between the shock and the turbulent boundary layer a small separation region is formed.

A <u>R</u>eynolds <u>S</u>tress <u>T</u>ransport <u>M</u>odel (RSTM) has been implemented into an explicit time-marching Runge-Kutta code. The equations for $\overline{u^2}, \overline{v^2}, \overline{uv}, k$ and ε, which are solved in an RSTM, are solved using an implicit solver which – unlike the Runge-Kutta solver – has proved to be very stable and reliable when solving these source-dominated transport equations.

The RSTM is superior to eddy viscosity turbulence models, mainly due to that the production terms need not to be modelled. In the paper it is shown that RSTM accounts for streamline curvature effects in a physically correct way, and that it responds properly to large irrotational strains.

Detailed comparisons of predictions and measurements are presented, and the following conclusions can be drawn:

- The agreement between predictions and measurements is, in general, good.
- The interaction between the shock and turbulent boundary layer is stronger in the predictions than in the experiments; this is attributed to *i)* that ahead of the shock the boundary layer is thicker in the predictions than in the experiments, *ii)* three-dimensional effects in the expriments.
- The ratio $\overline{u^2}/\overline{v^2} \simeq 12$ between the normal stresses in the shock region is surprisingly high; oscillations of the shock-wave observed in the experiments may explain this.

If the conclusion can be drawn that the oscillations in the shock-wave in the experimental flow are of considerable importance, it means, as pointed out in Ref. 26, that a numerical method capable of accounting for these unsteady phenomenon should be used. Using Large Eddy Simulation (LES) methods could be one future way to solve this type of flow.

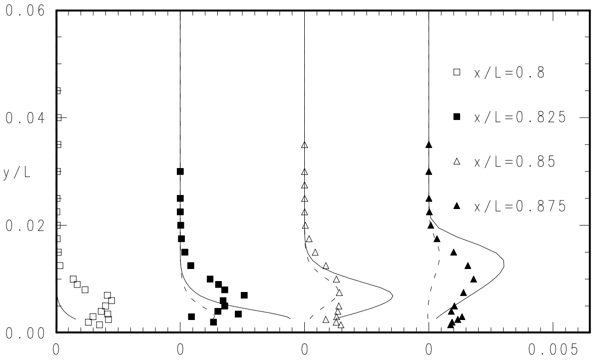

Figure 14: *Comparison of contribution to the production term* P_k *due to shear stress* $-\overline{uv}\partial U/\partial y$ *(solid line) and normal stresses* $-\left(\overline{u^2}-\overline{v^2}\right)\partial U/\partial x$ *(dashed lines). The experimental* $-\overline{uv}\partial U/\partial y$ *is also included (markers).*

Acknowledgements

Computer time at the CRAY-XMP at NSC (**N**ational **S**upercomputer **C**enter), Linköping, Sweden, is gratefully acknowledged.

References

[1] EUROVAL - A European Initiative on Validation of CFD-codes, W. Haase, F. Brandsma, E. Elsholz, M. Leschziner and D. Schwamborn (Eds.), Notes on Numerical Fluid Mechanics, Vieweg Verlag (to be published), 1993.

[2] BRADSHAW, P. – Effects of Streamline Curvature on Turbulent Flow, *AGARDograph*, no. 169, 1973.

[3] RODI, W. and SCHEUERER, G. – Calculation of Curved Shear Layers With Two-Equation Turbulence Models, *Phys. Fluids*, **26**, No. 6, pp. 1422-1435, 1983.

[4] THOMPSON, B.E. and WHITELAW, J.H. – Characteristics of a Trailing-Edge Flow With Turbulent Boundary-Layer Separation, *JFM*, **157**, pp. 305-326, 1985.

[5] RIZZI A. and MÜLLER, B. – Large-Scale Viscous Simulation of Laminar Vortex Flow Over a Delta Wing, *AIAA J.*, **27**, pp. 833- 840, 1989.

[6] MÜLLER, B. and RIZZI A. – Modelling of Turbulent Transonic Flow Around Airfoils and Wings, *Comm Appl Num Meth*, **6**, pp. 603-613, 1990.

[7] DAVIDSON, L. and RIZZI, A. — Navier-Stokes Stall Predictions Using an Algebraic Stress Model", *J. Spacecraft and Rockets*, Vol. 29(6), pp. 794-800, 1992 (see also AIAA-paper 92-0195, Reno, Jan. 1992).

[8] DAVIDSON, L. – Implementation of a Semi-Implicit $k-\varepsilon$ Turbulence Model in an Explicit Runge-Kutta Navier-Stokes Code, TR/RF/90/25, CERFACS, 1990.

[9] B. VAN LEER – Towards the Ultimate Conservative Difference Scheme. Monotonicity and Conservation Combined in a Second Order Scheme, *J. Comp. Phys.*, **14**, pp. 361-370, 1974.

[10] GIBSON, M.M. and LAUNDER, B.E. – Ground Effects on Pressure Fluctuations in the Atmospheric Boundary Layer, *J. Fluid Mech.*, **86**, pp. 491-512, 1978.

[11] DALY, B.J. and HARLOW, F.H., Transport equations of turbulence, *Phys. Fluids*, **13**, pp. 2634-2649, 1970.

[12] HUANG, P.G. and LESCHZINER, M.A. – Stabilisation of Recirculating-Flow Performed with Second-Moment Closures and Third-Order Discretization, 5th Turbulent Shear Flow, pp. 20.7-20.12, Cornell, 1985.

[13] WOLFSHTEIN, M. – The Velocity and Temperature Distribution in One-Dimensional Flow with Turbulence Augmentation and Pressure Gradient, *Int. J. Mass Heat Transfer*, **12**, pp. 301-318, 1969.

[14] CHEN, H.C. and PATEL, V.C. – Practical Near-Wall Turbulence Models for Complex Flows Including Separation, AIAA Paper No 87-1300, Honolulu, June 1987.

[15] GIBSON, M.M. and YOUNIS, B.A. – Calculation of Swirling Jets With a Reynolds Stress Closure, *Phys. Fluids*, **29**, pp. 38-48, 1986.

[16] CARETTA, L.S., GOSMAN, A.D., PATANKAR, S.V., SPALDING, D.B. – Two Calculation Procedures for Steady, Three-Dimensional Flows With Recirculation, Proc. Third Int. Conf. on Numerical Methods in Fluid Dynamics, Vol. 11, p. 60, ed. by Ehlers, Hepp and Weidemüller, 1972.

[17] PATANKAR, S.V. – Numerical Heat Transfer and Fluid Flow, McGraw-Hill, New York, 1980.

[18] DELERY, J., SIREIX, M. and CAPELIER, C. – ONERA, Rapport Technique No. 42/7078 AY 014, Chatillon, December 1980.

[19] DELERY, J. – Experimental Investigation of Turbulence Properties in Transonic Shock/Boundary-Layer Interactions, *AIAA J.*, **21**, pp. 180-185, 1983.

[20] DIMITRIADES, K.P. and LESCHZINER, M.A. – Computation of Shock/Turbulent-Boundary-Layer Interaction with Cell-Vertex Method and Two-Equation Turbulence Model, Proc. Int. Conf. on The Prediction and Exploitation of Separated Flow, London, 1989.

[21] LIEN, F.S. – Computational Modelling of 3D Flow in Complex Ducts and Passages, PhD thesis, University of Manchester, Manchester, 1992.

[22] LIEN, F.S. and LESCHZINER, M.A. – A Pressure-Correction Solution Strategy for Compressible Flow and its Application to Shock/Boundary-Layer Interaction Using Second-Moment Turbulence Closure, submitted to *J. Fluid Engng.*, 1992.

[23] DELERY, J. and MARVIN, J.G. – Shock-Wave Boundary Layer Interaction, Ed: E. Reshotko, AGARD-AG-280, 1986.

[24] DAVIDSON, L. – CERFACS' contribution in Task 3.2 to EUROVAL: A European Initiative on Validation of CFD-codes, W. Haase, F. Brandsma, E. Elsholz, M. Leschziner and D. Schwamborn (Eds.), Notes on Numerical Fluid Mechanics, Vieweg Verlag (to be published), 1993.

[25] PAGE, G. and LESCHZINER, M.A. – UMIST's contribution in Task 3.2 to EUROVAL: A European Initiative on Validation of CFD-codes, W. Haase, F. Brandsma, E. Elsholz, M. Leschziner and D. Schwamborn (Eds.), Notes on Numerical Fluid Mechanics, Vieweg Verlag (to be published), 1993.

[26] BENAY, R., CÖET, M.C. and DELERY, J. – A Study of Turbulence Modelling in Transonic Shock-Wave Boundary-Layer Interactions, Turbulent Shear Flows, Vol. 6, Selected Papers, pp. 194-214, Springer-Verlag, Berlin, 1989.

[27] ALBER, I.E., BACON, J.W., MASSON, B.S. and COLLINS, D.J. – An Experimental Investigation of Turbulent Transonic Viscous-Inviscid Interactions, *AIAA J.*, **11**, pp. 620-627, 1973.

[28] SEEGMILLER, H.L., MARWIN, J.G. and LEVY JR., L.L. – Steady and Unsteady Transonic Flow, *AIAA J.*, **16**, pp. 1262-1270, 1978.

[29] JOHNSON, D.A. and BACHALO, W.D. – Transonic Flow Past a Symmetrical Airfoil — Inviscid and Turbulent Flow Properties, *AIAA J.*, **18**, pp. 16-24, 1980.